HHS Public Access

Author manuscript

Magn Reson Med. Author manuscript; available in PMC 2023 July 12.

Published in final edited form as:

Magn Reson Med. 2021 November ; 86(5): 2635–2646. doi:10.1002/mrm.28875.

Temporal clustering, tissue composition, and total variation for mapping oxygen extraction fraction using QSM and quantitative BOLD

Junghun Cho[1], **Pascal Spincemaille**[1], **Thanh D. Nguyen**[1], **Ajay Gupta**[1], **Yi Wang**[1,2]

[1]Department of Radiology, Weill Cornell Medical College, New York, New York, USA

[2]Department of Biomedical Engineering, Cornell University, Ithaca, New York, USA

Abstract

Purpose: To improve the accuracy of quantitative susceptibility mapping plus quantitative blood oxygen level-dependent magnitude (QSM+qBOLD or QQ) based mapping of oxygen extraction fraction (OEF) and cerebral metabolic rate of oxygen (CMRO2) using temporal clustering, tissue composition, and total variation (CCTV).

Methods: Three-dimensional multi-echo gradient echo and arterial spin labeling images were acquired from 11 healthy subjects and 33 ischemic stroke patients. Diffusion-weighted imaging (DWI) was also obtained from patients. The CCTV mapping was developed for incorporating tissue-type information into clustering of the previous cluster analysis of time evolution (CAT) and applying total variation (TV). The QQ-based OEF and $CMRO_2$ were reconstructed with CAT, CAT+TV (CATV), and the proposed CCTV, and results were compared using region-of-interest analysis, Kruskal-Wallis test, and post hoc Wilcoxson rank sum test.

Results: In simulation, CCTV provided more accurate and precise OEF than CAT or CATV. In healthy subjects, QQ-based OEF was less noisy and more uniform with CCTV than CAT. In subacute stroke patients, OEF with CCTV had a greater contrast-to-noise ratio between DWI-defined lesions and the unaffected contralateral side than with CAT or CATV: 1.9 ± 1.3 versus 1.1 ± 0.7 ($P = .01$) versus 0.7 ± 0.5 ($P < .001$).

Conclusion: The CCTV mapping significantly improves the robustness of QQ-based OEF against noise.

Keywords

oxygen extraction fraction; quantitative blood oxygenation level-dependent imaging; quantitative susceptibility mapping; temporal clustering; tissue composition; total variation

Correspondence Yi Wang, Department of Radiology, Weill Cornell Medical College, MRI Research Institute, 407 East 61st St, RR-118, New York, NY 10065, USA. yiwang@med.cornell.edu.

SUPPORTING INFORMATION

Additional Supporting Information may be found online in the Supporting Information section.

1 | INTRODUCTION

Oxygen extraction fraction (OEF) and cerebral metabolic rate of oxygen ($CMRO_2$) are valuable for assessing brain tissue viability and function in neurological disorders including stroke and neurodegeneration.[1-4] In MRI, quantitative mapping of OEF and $CMRO_2$ has been developed by considering the strong paramagnetic effect of blood deoxyhemoglobin on (1) the magnitude signal, including calibrated functional MRI,[5-8] T_2-based methods,[9-12] and quantitative BOLD (qBOLD)[13-17]; and (2) the phase signal, such as whole-brain susceptometry-based oximetry[18-20] and quantitative susceptibility mapping (QSM)-based macrovascular[21-23] and microvascular[24-28] OEF mapping. A recent integrated model of QSM and qBOLD (QSM+qBOLD or QQ) can map OEF without vascular challenges by utilizing both magnitude and phase of multi-echo gradient-echo (mGRE) data,[29] a readily applicable sequence in any MRI system. Therefore, this QQ-based OEF mapping tool has great potential in clinical applications.

A major challenge in OEF mapping is its poorly conditioned nonconvex inversion nature that is sensitive to data noise.[16,30] The cluster analysis of time evolution (CAT) algorithm has improved effective SNR in the QQ approach.[31-34] To further suppress noise propagation in OEF, we integrate tissue-type information with CAT and apply total variation (TV) regularization in this study. Limited clusters using magnitude signal time evolution in CAT[31] may be improved by additional tissue type information, particularly gray matter (GM) versus white matter (WM), which helps to determine tissue-specific QQ model parameters including venous blood volume[35,36] and R_2.[17] Furthermore, TV regularization should help alleviate the propagation of measurement noise into the parameter map.[37] Accordingly, we propose to combine temporal clustering, tissue composition, and total variation (CCTV) for the QQ approach to OEF and $CMRO_2$ (with regional blood flow) mapping.

2 | THEORY

The $CMRO_2$ (μmol/100 g/min) can be estimated with $CMRO_2 = OEF \cdot CBF \cdot [H]_a$, where CBF is regional cerebral blood flow (mL/100 g/min) and $[H]_a = 7.377$ μmol/mL is the oxygenated heme molar concentration in an arteriole with hematocrit (Hct) = 0.357.[24]

The OEF can be defined as OEF = $1 - Y / Y_a$, where Y and Y_a (= 0.98[29]) are the venous and arterial oxygenation, respectively. For OEF estimation, the QQ model combines QSM (phase analysis) and qBOLD (magnitude analysis). Regularization R is imposed using a priori physiological constraints for robust parameter determination, such as suppressing noise propagation in the ill-posed $CMRO_2$ model inversion[25]:

$$Y^*, v^*, R_2^*, S_0^*, \chi_n^* = \underset{Y, v, R_2, S_0, \chi_{nb}}{\operatorname{argmin}} \left\{ w \left\| \chi - F_{QSM}(Y, v, \chi_n) \right\|_2^2 + \sum_j \left\| \left| S_j \right| - F_{qBOLD}(S_0, Y, v, R_2, \chi_n, t_j) \right\|_2^2 + R(Y) \right\}, \quad (1)$$

where w is weighting on the first QSM term.

The QSM term decomposes voxel-wise susceptibility (χ) into (1) blood susceptibility consisting of venous deoxyhemoglobin (i.e., OEF effect and fully oxygenated blood, $\chi_{ba} = -108.3$ ppb)[25] and (2) nonblood neural tissue susceptibility (χ_n) as follows:

$$F_{QSM}(Y, v, \chi_n) = \left[\psi_{Hb} \cdot \Delta\chi_{Hb} \cdot \left(-Y + \frac{1-(1-\alpha)\cdot Y_a}{\alpha}\right) + \frac{\chi_{ba}}{\alpha}\right] \cdot v + \left(1 - \frac{v}{\alpha}\right) \cdot \chi_n \quad (2)$$

where $\psi_{Hb} = 0.0909$ is the hemoglobin volume fraction assuming Hct = 0.357[26,38-40]; $\Delta\chi_{Hb} = 12522$ ppb is the susceptibility difference between deoxyhemoglobin and oxyhemoglobin[24,41]; $\alpha = 0.77$ is the ratio between the venous and total blood volumes[42]; and v is the venous blood volume fraction.

The second qBOLD term models magnitude signal, $|S_j|$, at the jth echo[29] as follows:

$$F_{qBOLD}(S_0, Y, v, R_2, \chi_n, t_j) = S_0 \cdot e^{-R_2 \cdot t_j} \cdot F_{BOLD}(Y, v, \chi_n, t_j) \cdot G(t_j) \quad (3)$$

where S_0 is signal intensity at $t_j = 0$; R_2 is the transverse relaxation rate; $F_{BOLD}(Y, v, \chi_n, t_j) = \exp[-v \cdot f_s(\delta\omega \cdot t_j)]$[16]; f_s is the signal decay due to the presence of blood vessel network whose asymptotic behavior is $f_s(\delta\omega \cdot t_j) \approx \frac{3}{10}(\delta\omega \cdot t_j)^2$ for $t_j \ll 1 / \delta\omega$ and $f_s(\delta\omega \cdot t_j) \approx \delta\omega \cdot t_j$ for $t_j \gg 1 / \delta\omega$[17]; and $\delta\omega(Y, \chi_n) = \frac{1}{3} \cdot \gamma \cdot B_0 \cdot [\psi_{Hb} \cdot \Delta\chi_{Hb} \cdot (1 - Y) + \chi_{ba} - \chi_n]$ is the characteristic frequency by the susceptibility difference between deoxygenated blood and the surrounding tissue,[29] in which $\gamma = 267.513$ (rad/s)/T; B_0 is the main magnetic field strength; and $G(t_j)$ is the macroscopic field inhomogeneity contribution to the mGRE signal estimated using the voxel spread function (see Appendix of Cho et al[29]).

In the previously introduced CAT method,[31] voxels with similar signal time evolution (F_{qBOLD} / G) form a cluster and are assumed to have similar tissue parameters (Y, v, R_2) for SNR improvement. In the proposed CCTV, tissue-type information is incorporated into the clusters obtained from CAT by dividing each cluster into its GM, WM, and cerebrospinal fluid (CSF) subcomponents, which can lead to comprehensive clustering using both temporal signal pattern and tissue-type information and to improved subsequent optimization initialization. In addition, as OEF is a linear function of Y ($OEF = 1 - Y / Y_a$ where $Y_a = 0.98$), the TV regularization, $R(Y) = \lambda \| \nabla Y \|_1$, is expected to suppress noise propagation into the OEF map by imposing spatial smoothness.[37]

3 | METHODS

3.1 | Numerical simulation

To compare the accuracy of QQ among CAT, CAT+TV (CATV), and CCTV, a simulation was performed similar to “Numerical Simulation 2” in Cho et al.[31] The average of the CAT, CATV, and CCTV results (a set of 3D Y, v, R_2, S_0, χ_n maps) from 1 real stroke patient (6 days following onset) was used as the ground truth. The mGRE and QSM values were then simulated using Equations 2 and 3 using this ground truth, with Gaussian noise added to obtain an SNR of 20. The noisy simulated data were processed using CAT,[31] CATV,

and CCTV, with the same optimization parameters and settings as in the experimental data. This was repeated 5 times for different instances of Gaussian noise to allow accuracy and precision measurement.

Additionally, to investigate the effect of the choice of ground truth on algorithm performance, the simulation was performed with four different ground truths (Supporting Information Table S1): case 1, CAT result; case 2, CATV result; case 3, CCTV result; and case 4, the average of the CAT, CATV, and CCTV results.

3.2 | Data acquisition

3.2.1 | Healthy subjects—This study was approved by the local institutional review board, and all subjects provided written consent. Without caffeine or alcohol intake 24 hours before MRI, 11 healthy adults (1 female, age 34 ± 12 years) underwent an MRI on a 3T scanner (HDxt; GE Healthcare, Waukesha, WI) in the resting state using (1) a 3D fast spin-echo arterial spin labeling (FSE ASL) sequence[43-45] (20-cm FOV, 1.56 × 1.56 × 3.5 mm^3 voxel size, 1500-ms labeling period, 1525-ms postlabel delay, 976.6-Hz/pixel bandwidth, spiral sampling of eight interleaves and 512 readout points per leaf, 35 axial slices, TE = 10.1 ms, TR = 4533 ms, and three signal averages), (2) a 3D spoiled mGRE sequence[46-48] with flow compensation in all three directions[48] (0.78 × 0.78 × 1.2 mm^3 voxel size, identical FOV to the 3D FSE ASL sequence, and seven equally spaced echoes: $TE_1/\Delta TE/TE_7$ = 2.3/3.9/25.8 ms, TR = 30.5 ms, bandwidth = 488.3 Hz/pixel, and flip angle = 15°), and (3) an inversion-prepared T_1-weighted spoiled gradient-echo sequence (BRAVO)[49] (0.78 × 0.78 × 1.2 mm^3, identical FOV to the 3D FSE ASL sequence, TE = 2.92 ms, TR = 7.69 ms, 450-ms prep time, bandwidth = Hz/pixel, and flip angle = 15°).

3.2.2 | Stroke patients—This retrospective image analysis was approved by the local institutional review board. Thirty-three ischemic stroke patients all with lesions in unilateral cerebral artery territory were classified into two groups based on the time interval between stroke onset and MRI scan[50]: acute (6-24 hours, $N = 6$) and subacute (1-14 days, $N = 27$) phase. They underwent MRI on a clinical 3T scanner (GE MR Discovery 750) using (1) 3D FSE ASL (24-cm FOV, 1.9 × 1.9 × 2.0 mm^3 voxel size, 1500-ms labeling period, 1525-ms postlabel delay, 976.6-Hz/pixel bandwidth, 68 axial slices, TE = 14.6 ms, TR = 4787 ms, and three signal averages), (2) 3D mGRE (0.47 × 0.47 × 2.0 mm^3 voxel size, identical FOV to the 3D FSE ASL sequence, and eight equally spaced echoes: $TE_1/\Delta TE/TE_8$ = 4.5/5/39.5 ms, TR = 42.8 ms, bandwidth = 244.1 Hz/pixel, and flip angle 20°), and (3) DWI (24-cm FOV; 0.94 × 0.94 × 3.2 mm^3 voxel size; 1953.1-Hz/pixel bandwidth; 0, 1000 s/mm^2 b-values; TE = 71 ms; TR = 3000 ms; and four signal averages), and (4) a T_1-weighted fluid attenuated inversion recovery sequence[51] (24-cm FOV, 0.5 × 0.5 × 5 mm^3 voxel size, TE = 23.4 ms, and TR = 1750 ms).

3.3 | Data processing: QSM and CBF

The QSM reconstruction comprised the total field estimation using an adaptive, quadratic fit of the mGRE phase,[48] local field calculation with the projection onto dipole fields (PDF) method,[47] and susceptibility estimation using the morphology-enabled dipole inversion with automatic uniform CSF zero-reference algorithm.[46,52-54] In stroke patients, the total field

was estimated using a linearfit of the mGRE phase,[55] as 3D flow compensation was not available on the clinical scanner. The CBF maps (mL/100 g/min) were generated from the ASL data using FuncTool (GE Healthcare). All images were co-registered and interpolated to the resolution of the QSM maps using the FSL FLIRT algorithm.[56,57]

3.4 | Data processing: OEF

The OEF map was estimated by QQ-CAT, QQ-CATV (QQ-CAT + TV), and the proposed QQ-CCTV. For CAT, the same OEF reconstruction as in the original CAT paper[31] was used, including clustering and optimization, except: (1) The regularization that average OEF for the whole brain should be similar to the brain OEF value estimated from the straight sinus vein was excluded, because this estimation is not based on a biophysics principle such as mass conservation; and (2) the v initial guess was set to 4/2/1% for GM/WM/CSF instead of 3/1.5/1%, to be consistent with the values from a similar mGRE-based method.[17] First, x-means clustering, a modified k-means with automatic optimal cluster number selection, was used on voxel-wise F_{qBOLD} / G. Cluster-based and voxel-wise optimization were performed consecutively to estimate the model parameters (Y, v, χ_n, R_2, S_0). For CATV, TV regularization ($\lambda\|\nabla Y\|_1$) was added to CAT with $\lambda = 2\times10^{-5}$ by L-curve analysis.[58]

For CCTV, each cluster from CAT was further separated into GM/WM/CSF subclusters using segmentation that was performed with T_1-weighting using the FSL FAST algorithm.[59] The same optimization procedure as CAT was used except setting the R_2 scaling factor to $avg(R_{2,0}) + 6.5\cdot SD(R_{2,0})$ instead of $avg(R_{2,0}) + 4\cdot SD(R_{2,0})$ to consider the decreased $SD(R_{2,0})$ due to the reduced cluster-wise number of voxels, where $avg(R_{2,0})$ and $SD(R_{2,0})$ denote the average and standard deviation (SD) of the R_2 initial guess in each cluster, respectively. The weights on QSM (w) and regularization (λ) were chosen by consecutive L-curve analysis[58]: $w = 2.5\times10^{-2}$ and $\lambda = 1\times10^{-5}$.

3.5 | Statistical analysis

In the numerical simulation, accuracy and precision were measured by mean absolute error (MAE $\equiv \frac{1}{N_v}\sum_{i=1}^{N_v} |OEF_{truth} - OEF_{avg}|$) and mean SD (MSD $\equiv \frac{1}{N_v}\sum_{i=1}^{N_v} OEF_{std}$), where $OEF_{avg} \equiv \frac{1}{N_t}\sum_{j=1}^{N_t} OEF_{i,j}$; $OEF_{std} \equiv \sqrt{\frac{1}{N_t}\sum_{j=1}^{N_t}\left(OEF_{i,j} - \frac{1}{N_t}\sum_{j=1}^{N_t} OEF_{i,j}\right)^2}$; is the voxel index; j is the trial index; N_v is the number of voxels; and N_t is the number of trials.

In healthy subjects, cortical GM (CGM) masks were constructed based on the inversion-prepared T_1-weighted spoiled gradient-echo image by an experienced neuroradiologist (A.G., 11 years of experience). To compare OEF and $CMRO_2$ values from QQ among CAT, CATV, and CCTV, region-of-interest analyses (mean and SD) were performed and, to assess statistical significance, Kruskal-Wallis (KW) tests and post hoc Wilcoxon rank sum (WRS) tests were performed. In the post hoc WRS tests, multiple-comparison correction was performed using the false discovery rate.[60] For stroke patients, regions of interest for the lesion and its corresponding contralateral side were drawn based on DWI by the same neuroradiologist. The detectability of lesion OEF abnormality was measured by the contrast-to-noise ratio (CNR) between the lesion and the contralateral side

($CNR \equiv \frac{|\overline{OEF_{lesion}} - \overline{OEF_{contralateral\,side}}|}{\sigma(OEF_{contralateral\,side})}$), assuming that OEF variation within the contralateral side originated from noise. The CNR was compared among CAT, CATV, and CCTV using KW tests and post hoc WRS tests. A p-value less than .05 was considered significant.

4 | RESULTS

Figure 1 shows the OEF comparison between QQ-CAT, QQ-CATV, and QQ-CCTV in the simulated stroke brain (numerical simulation). The QQ-CCTV provided the most accurate OEF map (smallest MAE: 5.3 vs 5.4 vs 4.3%) with the highest precision (smallest MSD: 3.1 vs 2.4, and 1.8%). The OEF_{avg} map from QQ-CCTV best captured low OEF values in the lesion (smallest MAE in the lesion: 3.4 vs 3.5 vs 2.8%). In the investigation of the effect of the choice of ground truth on algorithm performance, QQ-CCTV provided the highest accuracy for cases 1, 3, and 4 and highest precision for all cases (Supporting Information Table S1).

Figure 2 shows a comparison of QQ among CAT, CATV, and CCTV in a healthy subject. Compared with QQ-CAT, QQ-CCTV showed a less noisy and more uniform OEF map and subsequently a less noisy $CMRO_2$ map. The v map from QQ-CCTV showed a clear CGM/WM difference. In the CGM of healthy subjects, QQ-CCTV provided greater v than QQ-CAT and QQ-CATV (Supporting Information Figure S1). For QQ-CAT, QQ-CATV, and QQ-CCTV, the OEF value was 34.2 ± 5.5, 34.5 ± 7.1, and 30.6 ± 3.1% (P = .17, KW test); $CMRO_2$ was 154.5 ± 25.6, 156.6 ± 33.2, and 139.2 ± 23.9 μmol/100 g/min (P = .24, KW test); v was 1.4 ± 0.3 (P = .002, WRS test), 1.4 ± 0.4 (P = .002, WRS test), and 2.7 ± 0.5%; R_2 was 16.2 ± 0.6, 16.2 ± 0.6, and 15.8 ± 0.6 Hz (P = .23, KW test); and χ_n was −21.3 ± 7.8, −21.3 ± 7.7, and −24.0 ± 7.8 ppb (P = .41, KW test).

Figure 3 shows representative OEF maps from QQ-CAT, QQ-CATV, and QQ-CCTV in ischemic stroke patients. Compared with QQ-CAT and QQ-CATV, QQ-CCTV showed an improved spatial overlap between low OEF regions and a DWI-defined lesion in the subacute phase with less noisy OEF maps (Figure 4).

Figure 5 shows a boxplot of OEF CNR between the lesion and contralateral side in ischemic stroke patients. Compared with QQ-CAT and QQ-CATV, QQ-CCTV provided significantly greater OEF CNR in the subacute phase (1.9 ± 1.3 vs 1.1 ± 0.7 [P = .01, WRS test] vs 0.7 ± 0.5 [P < .001, WRS test]), but showed similar CNR in the acute phase (0.5 ± 0.4 vs 0.7 ± 0.4 vs 0.6 ± 0.5 [P = .83, KW test]).

5 | DISCUSSION

Our results indicate that CCTV substantially suppresses noise propagation into QQ-based OEF mapping. Compared with the previous CAT algorithm, the OEF map estimated by CCTV demonstrates greater accuracy and precision in simulation, appears less noisy and more uniform in healthy subjects, and detects OEF abnormalities better in stroke patients. Hence, CCTV provides robust QQ-based OEF mapping without vascular challenges from widely available mGRE data.

Complementary to the magnitude mGRE modeling,[13] OEF content from phase data through QSM processing[24] is valuable due to QSM sensitivity to tissue iron.[61,62] The QQ approach represents a full use of mGRE data,[29] but denoising is still critical[31] because its poor-conditioned nonconvex inversion is prone to data noise. Compared with CAT, CATV and CCTV show less noisy and more uniform OEF maps (Figures 2 and 3), which agree with the reference standard ^{15}O PET-OEF.[63,64] The OEF noise suppression may result from using TV regularization, which reduces Gaussian noise[37] and MRI artifacts including streaking[65] and Gibbs ringing.[66] It also agrees with the suppressed Gaussian noise propagation on OEF in numerical simulation using TV (Figure 1). Additionally, in CCTV, the incorporation of tissue-type information may lead to more robust inversion with improved initialization and inversion condition.

The QQ-CCTV technique shows smaller OEF values than QQ-CAT and QQ-CATV (Figure 2 and Supporting Figure S1), 34.5 ± 7.1% vs 30.6 ± 3.1% in CGM (although the difference was not significant [uncorrected $P = .09$, WRS test]), which are accompanied by higher v (1.4 ± 0.4% and 2.7 ± 0.5% [$P < .001$, WRS test]). This can be explained because, for the same measured magnitude signal decay and susceptibility, OEF decreases if v increases (Equations 2 and 3). The OEF values with CAT, CATV, and CCTV are consistent with MRI OEF values reported in the literature (e.g., 26 ± 2%,[9] 29 ± 3%,[67] 31.7 ± 6.1%,[68] and 35 ± 4%).[6] Furthermore, the v from QQ-CCTV falls into previously reported MRI-based v values (e.g., 2.46 ± 0.28%,[42] 2.68 ± 0.47%,[69] and 3.6 ± 0.4%).[70] Also, the clear CGM/WM contrast from QQ-CCTV is in line with the v contrast in MRI literature[35,36] and may be caused by tissue-type (GM/WM) integration into clustering, which leads to a more realistic v initialization in optimization. The R_2 in CGM estimated with CAT, CATV, and CCTV (16.2 ± 0.6 Hz, 16.2 ± 0.6 Hz, and 15.8 ± 0.6 Hz) agree with the values from other MR techniques (15.1 ± 0.6 Hz[17] and 17.1 ± 2 Hz).[71]

In the subacute ischemic stroke patients (Figure 3), low OEF regions from QQ-CCTV agree better with DWI-defined lesions without severe artifacts compared with CAT or CATV. For instance, in a 9-day post-onset case (Figure 4), the low OEF region with CCTV largely coincided with the DWI-defined lesion, whereas CAT and CATV did not depict low OEF values clearly in the lesion and showed noise and artifacts in OEF maps. This is consistent with the significantly greater OEF CNR from CCTV compared with CAT and CATV in the subacute phase (1.9 ± 1.3 vs 1.1 ± 0.7 [$P = .01$, WRS test] and 0.7 ± 0.5 [$P < .001$, WRS test]) (Figure 5), which suggests better detection of OEF abnormalities. The improved OEF CNR may result from improved decoupling between OEF and v, a crucial issue in qBOLD-based OEF modeling without very high SNR.[16] The improved decoupling may result from noise propagation suppression into OEF, using TV regularization and proper v initialization by integrating tissue-type information into clustering (Figure 4). In the acute phase (Figure 3), lesion OEF values appear similar to those on the contralateral side, which suggests that an acute lesion tissue may be salvageable.

Compared to CAT with whole-brain average OEF regularization as in the original CAT paper,[31] CATV provided greater precision (smaller MSD: 2.8 vs 2.4%) in the simulation, lower OEF SD within the CGM of healthy subjects (5.9 ± 1.8 vs 3.2 ± 1.4%; $P = .02$; WRS

test), and contralateral side in the subacute phase stroke patients (6.7 ± 3.2 vs 4.8 ± 2.7%; $P < .001$; WRS test). This suggests that TV is more effective to suppress noise propagation into OEF than the whole-brain average OEF regularization.

Among 6 acute ischemic stroke patients, 3 showed the diffusion/perfusion (DWI/CBF) mismatch region, potentially salvageable tissue or penumbra[72-74] (Supporting Information Figure S2). In the OEF maps obtained by QQ-CCTV, the hemisphere containing the lesion showed a higher average OEF than the contralateral hemisphere when the CBF deficit volume was substantially larger than the DWI-defined lesion volume; for example, the average OEF ratio between ipsilateral and contralateral hemisphere was 1.1 when the volume fraction of the DWI/CBF mismatched region relative to the DWI-defined lesion was 19.8 (24 hours post-onset case in Supporting Information Figure S2). This is consistent with previous acute ischemic stroke studies where, as blood flow decreases, OEF in the ipsilateral hemisphere may be elevated pathologically to maintain normal oxygen metabolism when autoregulatory capacity is exceeded.[75-77] However, the sample size ($N = 3$) was too small to make any meaningful inferences. In addition, low lesion OEF values in the subacute stroke patients (Figure 3) may indicate irreversibly damaged tissue.

There are limitations in this study that warrant further investigation. First, clustering assumes that voxels with similar signal decay patterns would have similar model parameter values, including OEF. As an extreme case, voxels with identical QSM and mGRE magnitude would have the same model parameter value based on Equations 2 and 3. Clustering is critical, as very high SNR, (e.g., 500) is required for reasonable parameter estimation,[16] and clustering improves the effective SNR substantially.[31] As different tissue types show different mGRE signal decay patterns (e.g., different R_2 between GM/WM),[17] clustering may be a realistic and reasonable assumption. However, its validity has not been thoroughly investigated, which remains a topic for future study. Even if the clustering assumption is valid, the resultant OEF accuracy may depend on clustering performance. For clustering in this study, x-means was used to choose the optimal number of clusters based on Bayesian information criteria.[78] The clustering result may vary with the used metric, (e.g., Akaike information criterion) or method (e.g., hierarchical clustering).[79,80] Voxel-wise optimization can be performed after cluster-wise optimization to alleviate the consequences of imperfect clustering, and the resultant OEF maps are not sensitive to the number of clusters in K-means clustering.[31] Second, as large veins are treated identical to brain tissue, their OEF and v estimations may be inaccurate. This could be alleviated by imposing $v = 1$ for large veins. Third, as flow compensation was not available in the stroke patients, the oxygenation in large veins may be overestimated without considering phase errors caused by flow motion.[48] This may lead to underestimation in the whole-brain average OEF, because OEF was initialized using venous oxygenation in a main draining vein, such as the straight sinus. Fourth, a fixed Hct value due to the lack of its measurement in this study may lead to errors in OEF estimation. Tissue Hct was set to 0.357 for all subjects, which corresponds to large-vessel Hct of 0.49,[38] although large-vessel Hct values vary among subjects and are higher in males (0.42~0.52) than females (0.37~0.47).[81,82] Therefore, the fixed Hct assumption may result in an inaccurate OEF estimation, as the hemoglobin volume fraction, ψ_{Hb}, determined by Hct, is coupled with venous oxygenation, Y (Equations 2 and 3). Fifth,

in numerical simulation, the algorithm's performance (CAT, CATV, and CCTV) may be different if a different ground truth is used, because all three algorithms may still depend on optimization details such as the initial guess. To minimize this bias, the average of CAT, CATV, and CCTV results was used as the ground truth in this study. Additionally, the effect of the choice of ground truth on algorithm performance was investigated by performing the simulation with four different sets of ground truth (Supporting Information Table S1): case 1, CAT result; case 2, CATV result; case 3, CCTV result; and case 4, the average of CCTV, CAT, and CATV results (shown in Figure 1). CCTV generally outperformed the other two algorithms by providing the highest accuracy (smallest MAE) for cases 1, 3, and 4 and the highest precision (smallest MSD) for all cases. Finally, QQ-CCTV optimization is still nonconvex, so convergence may be influenced by solver implementation, parameter scaling, initial guess, and stopping criterion. As in most machine-learning techniques that involve empirical parameters, an implemented QQ-CCTV needs to be not only verified with simulation data as done here, but also validated against a reference standard such as ^{15}O PET[32] and evaluated with respect to repeatability and reproducibility[83] for clinical applications such as studies over all age groups.[84]

6 | CONCLUSIONS

With the significantly improved accuracy by integrated temporal and tissue-type clustering and total variation denoising, the proposed QQ-CCTV method can be readily applied to study tissue viability in neurologic disorders including ischemic stroke,[23], Alzheimer's disease,[85,86] multiple sclerosis,[87] and tumor.[88]

Supplementary Material

Refer to Web version on PubMed Central for supplementary material.

ACKNOWLEDGMENT

The authors thank Kelly Gillen, PhD, for her assistance with the manuscript editing.

Funding information

National Institutes of Health, Grant/Award Number: R01NS090464, R01NS095562, R21AG067466, S10OD021782, R01NS105144 and K99NS123229

REFERENCES

1. Derdeyn CP, Videen TO, Yundt KD, et al. Variability of cerebral blood volume and oxygen extraction: stages of cerebral haemodynamic impairment revisited. Brain. 2002;125:595–607. [PubMed: 11872616]
2. Gupta A, Baradaran H, Schweitzer AD, et al. Oxygen extraction fraction and stroke risk in patients with carotid stenosis or occlusion: a systematic review and meta-analysis. Am J Neuroradiol. 2014;35:250–255. [PubMed: 23945227]
3. Gupta A, Chazen JL, Hartman M, et al. Cerebrovascular reserve and stroke risk in patients with carotid stenosis or occlusion: a systematic review and meta-analysis. Stroke. 2012;43:2884–2891. [PubMed: 23091119]

4. Silverman DH, Small GW, Chang CY, et al. Positron emission tomography in evaluation of dementia: regional brain metabolism and long-term outcome. JAMA. 2001;286:2120–2127. [PubMed: 11694153]
5. Bulte DP, Kelly M, Germuska M, et al. Quantitative measurement of cerebral physiology using respiratory-calibrated MRI. Neuroimage. 2012;60:582–591. [PubMed: 22209811]
6. Gauthier CJ, Hoge RD. Magnetic resonance imaging of resting OEF and CMRO2 using a generalized calibration model for hypercapnia and hyperoxia. Neuroimage. 2012;60:1212–1225. [PubMed: 22227047]
7. Hoge RD. Calibrated fMRI. Neuroimage. 2012;62:930–937. [PubMed: 22369993]
8. Wise RG, Harris AD, Stone AJ, Murphy K. Measurement of OEF and absolute CMRO 2: MRI-based methods using interleaved and combined hypercapnia and hyperoxia. Neuroimage. 2013;83:135–147. [PubMed: 23769703]
9. Bolar DS, Rosen BR, Sorensen A, Adalsteinsson E. Quantitative Imaging of extraction of oxygen and Tissue consumption (QUIXOTIC) using venular-targeted velocity-selective spin labeling. Magn Reson Med. 2011;66:1550–1562. [PubMed: 21674615]
10. Guo J, Wong EC. Venous oxygenation mapping using velocity-selective excitation and arterial nulling. Magn Reson Med. 2012;68:1458–1471. [PubMed: 22294414]
11. Lu H, Ge Y. Quantitative evaluation of oxygenation in venous vessels using T2-relaxation-under-spin-tagging MRI. Magn Reson Med. 2008;60:357–363. [PubMed: 18666116]
12. Jiang D, Deng S, Franklin CG, et al. Validation of T2-based oxygen extraction fraction measurement with ^{15}O positron emission tomography. Magn Reson Med. 2021;85:290–297. [PubMed: 32643207]
13. Yablonskiy DA, Haacke EM. Theory of NMR signal behavior in magnetically inhomogeneous tissues: the static dephasing regime. Magn Reson Med. 1994;32:749–763. [PubMed: 7869897]
14. He X, Yablonskiy DA. Quantitative BOLD: mapping of human cerebral deoxygenated blood volume and oxygen extraction fraction: default state. Magn Reson Med. 2007;57:115–126. [PubMed: 17191227]
15. He X, Zhu M, Yablonskiy DA. Validation of oxygen extraction fraction measurement by qBOLD technique. Magn Reson Med. 2008;60:882–888. [PubMed: 18816808]
16. Yablonskiy DA, Sukstanskii AL, He X. BOLD-based techniques for quantifying brain hemodynamic and metabolic properties—theoretical models and experimental approaches. NMR Biomed. 2013;26:963–986. [PubMed: 22927123]
17. Ulrich X, Yablonskiy DA. Separation of cellular and BOLD contributions to T2* signal relaxation. Magn Reson Med. 2016;75:606–615. [PubMed: 25754288]
18. Jain V, Langham MC, Wehrli FW. MRI estimation of global brain oxygen consumption rate. J Cereb Blood Flow Metab. 2010;30:1598–1607. [PubMed: 20407465]
19. Wehrli FW, Rodgers ZB, Jain V, et al. Time-resolved MRI oximetry for quantifying CMRO(2) and vascular reactivity. Acad Radiol. 2014;21:207–214. [PubMed: 24439334]
20. Wehrli FW, Fan AP, Rodgers ZB, Englund EK, Langham MC. Susceptibility-based time-resolved whole-organ and regional tissue oximetry. NMR Biomed. 2017;30:e3495.
21. Fan AP, Benner T, Bolar DS, Rosen BR, Adalsteinsson E. Phase-based regional oxygen metabolism (PROM) using MRI. Magn Reson Med. 2012;67:669–678. [PubMed: 21713981]
22. Fan AP, Bilgic B, Gagnon L, et al. Quantitative oxygenation venography from MRI phase. Magn Reson Med. 2014;72:149–159. [PubMed: 24006229]
23. Kudo K, Liu T, Murakami T, et al. Oxygen extraction fraction measurement using quantitative susceptibility mapping: comparison with positron emission tomography. J Cereb Blood Flow Metab. 2016;36:1424–1433. [PubMed: 26661168]
24. Zhang J, Liu T, Gupta A, Spincemaille P, Nguyen TD, Wang Y. Quantitative mapping of cerebral metabolic rate of oxygen (CMRO2) using quantitative susceptibility mapping (QSM). Magn Reson Med. 2015;74:945–952. [PubMed: 25263499]
25. Zhang J, Zhou D, Nguyen TD, Spincemaille P, Gupta A, Wang Y. Cerebral metabolic rate of oxygen (CMRO2) mapping with hyperventilation challenge using quantitative susceptibility mapping (QSM). Magn Reson Med. 2017;77:1762–1773. [PubMed: 27120518]

26. Zhang J, Cho J, Zhou D, et al. Quantitative susceptibility mapping-based cerebral metabolic rate of oxygen mapping with minimum local variance. Magn Reson Med. 2018;79:172–179. [PubMed: 28295523]
27. Ma Y, Mazerolle EL, Cho J, Sun H, Wang Y, Pike GB. Quantification of brain oxygen extraction fraction using QSM and a hyperoxic challenge. Magn Reson Med. 2020;84:3271–3285. [PubMed: 32602975]
28. Ma Y, Sun H, Cho J, Mazerolle EL, Wang Y, Pike GB. Cerebral OEF quantification: a comparison study between quantitative susceptibility mapping and dual-gas calibrated BOLD imaging. Magn Reson Med. 2020;83:68–82. [PubMed: 31373088]
29. Cho J, Kee Y, Spincemaille P, et al. Cerebral metabolic rate of oxygen (CMRO2) mapping by combining quantitative susceptibility mapping (QSM) and quantitative blood oxygenation level-dependent imaging (qBOLD). Magn Reson Med. 2018;80:1595–1604. [PubMed: 29516537]
30. Lee H, Englund EK, Wehrli FW. Interleaved quantitative BOLD: combining extravascular R2'- and intravascular R2-measurements for estimation of deoxygenated blood volume and hemoglobin oxygen saturation. Neuroimage. 2018;174:420–431. [PubMed: 29580967]
31. Cho J, Zhang S, Kee Y, et al. Cluster analysis of time evolution (CAT) for quantitative susceptibility mapping (QSM) and quantitative blood oxygen level-dependent magnitude (qBOLD)-based oxygen extraction fraction (OEF) and cerebral metabolic rate of oxygen (CMRO2) mapping. Magn Reson Med. 2020;83:844–847. [PubMed: 31502723]
32. Cho J, Lee J, An H, Goyal MS, Su Y, Wang Y. Cerebral oxygen extraction fraction (OEF): comparison of challenge-free gradient echo QSM+qBOLD (QQ) with 15O PET in healthy adults. J Cereb Blood Flow Metab. 2020:1–11. 10.1177/0271678X20973951
33. Cho J, Ma Y, Spincemaille P, Pike GB, Wang Y. Cerebral oxygen extraction fraction: comparison of dual-gas challenge calibrated BOLD with CBF and challenge-free gradient echo QSM+qBOLD. Magn Reson Med. 2021;85:953–961. [PubMed: 32783233]
34. Zhang S, Cho J, Nguyen TD, et al. Initial experience of challenge-free MRI-based oxygen extraction fraction mapping of ischemic stroke at various stages: comparison with perfusion and diffusion mapping. Front Neurosci. 2020;14:949–959.
35. Lee H, Wehrli FW. Venous cerebral blood volume mapping in the whole brain using venous-spin-labeled 3D turbo spin echo. Magn Reson Med. 2020;84:1991–2003. [PubMed: 32243708]
36. Blockley NP, Griffeth VEM, Germuska MA, Bulte DP, Buxton RB. An analysis of the use of hyperoxia for measuring venous cerebral blood volume: comparison of the existing method with a new analysis approach. Neuroimage. 2013;72:33–40. [PubMed: 23370053]
37. Rudin LI, Osher S, Fatemi E. Nonlinear total variation based noise removal algorithms. Physica D. 1992;60:259–268.
38. Sakai F, Nakazawa K, Tazaki Y, et al. Regional cerebral blood volume and hematocrit measured in normal human volunteers by single-photon emission computed tomography. J Cereb Blood Flow Metab. 1985;5:207–213. [PubMed: 3921557]
39. Savicki JP, Lang G, Ikeda-Saito M. Magnetic susceptibility of oxy- and carbonmonoxyhemoglobins. Proc Natl Acad Sci. 1984;81:5417–5419. [PubMed: 6591198]
40. Hoffman R. Hematology: Basic Principles and Practice. London, United Kingdom: Churchill Livingstone; 2005.
41. Spees WM, Yablonskiy DA, Oswood MC, Ackerman JJ. Water proton MR properties of human blood at 1.5 Tesla: magnetic susceptibility, T(1), T(2), T*(2), and non-Lorentzian signal behavior. Magn Reson Med. 2001;45:533–542. [PubMed: 11283978]
42. Hongyu A, Weili L. Cerebral venous and arterial blood volumes can be estimated separately in humans using magnetic resonance imaging. Magn Reson Med. 2002;48:583–588. [PubMed: 12353273]
43. Dai W, Garcia D, de Bazelaire C, Alsop DC. Continuous flow-driven inversion for arterial spin labeling using pulsed radio frequency and gradient fields. Magn Reson Med. 2008;60:1488–1497. [PubMed: 19025913]
44. Alsop DC, Detre JA, Golay X, et al. Recommended implementation of arterial spin-labeled perfusion MRI for clinical applications: a consensus of the ISMRM perfusion study group and

the European consortium for ASL in dementia. Magn Reson Med. 2015;73:102–116. [PubMed: 24715426]

45. Buxton RB, Frank LR, Wong EC, Siewert B, Warach S, Edelman RR. A general kinetic model for quantitative perfusion imaging with arterial spin labeling. Magn Reson Med. 1998;40:383–396. [PubMed: 9727941]
46. Wang Y, Liu T. Quantitative susceptibility mapping (QSM): decoding MRI data for a tissue magnetic biomarker. Magn Reson Med. 2015;73:82–101. [PubMed: 25044035]
47. Liu T, Khalidov I, de Rochefort L, et al. A novel background field removal method for MRI using projection onto dipole fields (PDF). NMR Biomed. 2011;24:1129–1136. [PubMed: 21387445]
48. Xu B, Liu T, Spincemaille P, Prince M, Wang Y. Flow compensated quantitative susceptibility mapping for venous oxygenation imaging. Magn Reson Med. 2014;72:438–445. [PubMed: 24006187]
49. Mugler JP 3rd, Brookeman JR. Three-dimensional magnetization-prepared rapid gradient-echo imaging (3D MP RAGE). Magn Reson Med. 1990;15:152–157. [PubMed: 2374495]
50. Fung SH, Roccatagliata L, Gonzalez RG, Schaefer PW. MR diffusion imaging in ischemic stroke. Neuroimaging Clin N Am. 2011;21:345–377, xi. [PubMed: 21640304]
51. Hori M, Okubo T, Uozumi K, Ishigame K, Kumagai H, Araki T. T1-weighted fluid-attenuated inversion recovery at low field strength: a viable alternative for T1-weighted intracranial imaging. Am J Neuroradiol. 2003;24:648–651. [PubMed: 12695197]
52. de Rochefort L, Liu T, Kressler B, et al. Quantitative susceptibility map reconstruction from MR phase data using bayesian regularization: validation and application to brain imaging. Magn Reson Med. 2010;63:194–206. [PubMed: 19953507]
53. Liu J, Liu T, de Rochefort L, et al. Morphology enabled dipole inversion for quantitative susceptibility mapping using structural consistency between the magnitude image and the susceptibility map. Neuroimage. 2012;59:2560–2568. [PubMed: 21925276]
54. Liu Z, Spincemaille P, Yao Y, Zhang Y, Wang Y. MEDI+0: morphology enabled dipole inversion with automatic uniform cerebrospinal fluid zero reference for quantitative susceptibility mapping. Magn Reson Med. 2018;79:2795–2803. [PubMed: 29023982]
55. Liu T, Wisnieff C, Lou M, Chen W, Spincemaille P, Wang Y. Nonlinear formulation of the magnetic field to source relationship for robust quantitative susceptibility mapping. Magn Reson Med. 2013;69:467–476. [PubMed: 22488774]
56. Jenkinson M, Smith S. A global optimisation method for robust affine registration of brain images. Med Image Anal. 2001;5:143–156. [PubMed: 11516708]
57. Jenkinson M, Bannister P, Brady M, Smith S. Improved optimization for the robust and accurate linear registration and motion correction of brain images. Neuroimage. 2002;17:825–841. [PubMed: 12377157]
58. Hansen PC. Analysis of discrete Ill-posed problems by means of the L-curve. SIAM Rev. 1992;34:561–580.
59. Zhang Y, Brady M, Smith S. Segmentation of brain MR images through a hidden Markov random field model and the expectation-maximization algorithm. IEEE Trans Med Imaging. 2001;20:45–57. [PubMed: 11293691]
60. Benjamini Y, Hochberg Y. Controlling the false discovery rate: a practical and powerful approach to multiple testing. J Roy Stat Soc: Ser B (Methodol). 1995;57:289–300.
61. Stüber C, Pitt D, Wang Y. Iron in multiple sclerosis and its noninvasive imaging with quantitative susceptibility mapping. Int J Mol Sci. 2016;17:100. [PubMed: 26784172]
62. Kirui DK, Khalidov I, Wang Y, Batt CA. Targeted near-IR hybrid magnetic nanoparticles for in vivo cancer therapy and imaging. Nanomed Nanotechnol Biol Med. 2013;9:702–711.
63. Mintun MA, Raichle ME, Martin WR, Herscovitch P. Brain oxygen utilization measured with O-15 radiotracers and positron emission tomography. J Nucl Med. 1984;25:177–187. [PubMed: 6610032]
64. Raichle ME, MacLeod AM, Snyder AZ, Powers WJ, Gusnard DA, Shulman GL. A default mode of brain function. Proc Natl Acad Sci. 2001;98:676–682. [PubMed: 11209064]

65. Block KT, Uecker M, Frahm J. Undersampled radial MRI with multiple coils. Iterative image reconstruction using a total variation constraint. Magn Reson Med. 2007;57:1086–1098. [PubMed: 17534903]
66. Block KT, Uecker M, Frahm J. Suppression of MRI truncation artifacts using total variation constrained data extrapolation. Int J Biomed Imaging. 2008;2008:184123. [PubMed: 18784847]
67. Fan AP, Schäfer A, Huber L, et al. Baseline oxygenation in the brain: correlation between respiratory-calibration and susceptibility methods. Neuroimage. 2016;125:920–931. [PubMed: 26549301]
68. Christen T, Schmiedeskamp H, Straka M, Bammer R, Zaharchuk G. Measuring brain oxygenation in humans using a multiparametric quantitative blood oxygenation level dependent MRI approach. Magn Reson Med. 2012;68:905–911. [PubMed: 22162074]
69. An H, Lin W. Cerebral oxygen extraction fraction and cerebral venous blood volume measurements using MRI: effects of magnetic field variation. Magn Reson Med. 2002;47:958–966. [PubMed: 11979575]
70. Stone AJ, Blockley NP. A streamlined acquisition for mapping baseline brain oxygenation using quantitative BOLD. Neuroimage. 2017;147:79–88. [PubMed: 27915118]
71. Domsch S, Mie MB, Wenz F, Schad LR. Non-invasive multiparametric qBOLD approach for robust mapping of the oxygen extraction fraction. Zeitschrift für Medizinische Physik. 2014;24:231–242. [PubMed: 24743060]
72. Neumann-Haefelin T, Wittsack HJ, Wenserski F, et al. Diffusion- and perfusion-weighted MRI. The DWI/PWI mismatch region in acute stroke. Stroke. 1999;30:1591–1597. [PubMed: 10436106]
73. Dirnagl U, Iadecola C, Moskowitz MA. Pathobiology of ischaemic stroke: an integrated view. Trends Neurosci. 1999;22:391–397. [PubMed: 10441299]
74. Heiss WD. The concept of the penumbra: can it be translated to stroke management? Int J Stroke. 2010;5:290–295. [PubMed: 20636712]
75. Fan AP, Khalil AA, Fiebach JB, et al. Elevated brain oxygen extraction fraction measured by MRI susceptibility relates to perfusion status in acute ischemic stroke. J Cereb Blood Flow Metab. 2020;40:539–551. [PubMed: 30732551]
76. Liu Z, Li Y. Cortical cerebral blood flow, oxygen extraction fraction, and metabolic rate in patients with middle cerebral artery stenosis or acute stroke. AJNR Am J Neuroradiol. 2016;37:607–614. [PubMed: 26680459]
77. Xie S, Hui LH, Xiao JX, Zhang XD, Peng Q. Detecting misery perfusion in unilateral steno-occlusive disease of the internal carotid artery or middle cerebral artery by MR imaging. AJNR Am J Neuroradiol. 2011;32:1504–1509. [PubMed: 21700788]
78. Pelleg D, Moore AW. X-means: extending K-means with efficient estimation of the number of clusters. In: Proceedings of the 17th International Conference on Machine Learning, Stanford, California, 2000. pp 727–734.
79. Jain AK. Data clustering: 50 years beyond K-means. Pattern Recogn Lett. 2010;31:651–666.
80. Wilks DS. Cluster analysis. In: Wilks DS, editor. International Geophysics. Volume 100, Chapter 15. Cambridge, MA: Academic Press; 2011. pp 603–616.
81. Cohen E, Kramer M, Shochat T, Goldberg E, Krause I. Relationship between hematocrit levels and intraocular pressure in men and women: a population-based cross-sectional study. Medicine. 2017;96:e8290. [PubMed: 29019901]
82. Murphy WG. The sex difference in haemoglobin levels in adults—mechanisms, causes, and consequences. Blood Rev. 2014;28:41–47. [PubMed: 24491804]
83. Deh K, Nguyen TD, Eskreis-Winkler S, et al. Reproducibility of quantitative susceptibility mapping in the brain at two field strengths from two vendors. J Magn Reson Imaging. 2015;42:1592–1600. [PubMed: 25960320]
84. Persson N, Wu J, Zhang Q, et al. Age and sex related differences in subcortical brain iron concentrations among healthy adults. Neuroimage. 2015;122:385–398. [PubMed: 26216277]
85. Sun X, He G, Qing H, et al. Hypoxia facilitates Alzheimer's disease pathogenesis by up-regulating BACE1 gene expression. Proc Natl Acad Sci U S A. 2006;103:18727–18732. [PubMed: 17121991]

86. Acosta-Cabronero J, Williams GB, Cardenas-Blanco A, Arnold RJ, Lupson V, Nestor PJ. In vivo quantitative susceptibility mapping (QSM) in Alzheimer's disease. PLoS One. 2013;8:e81093. [PubMed: 24278382]

87. Trapp BD, Stys PK. Virtual hypoxia and chronic necrosis of demyelinated axons in multiple sclerosis. Lancet Neurol. 2009;8:280–291. [PubMed: 19233038]

88. Stadlbauer A, Zimmermann M, Kitzwogerer M, et al. MR imaging-derived oxygen metabolism and neovascularization characterization for grading and IDH gene mutation detection of gliomas. Radiology. 2017;283:799–809. [PubMed: 27982759]

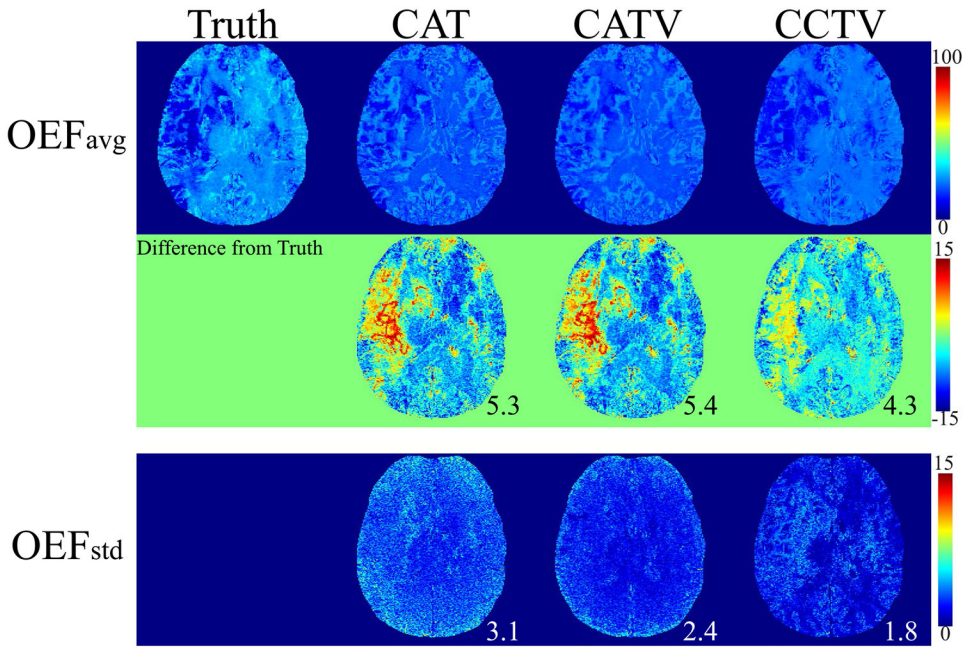

FIGURE 1.

Comparison between the oxygen extraction fraction (OEF) obtained by QQ (QSM + qBOLD) CAT (cluster analysis of time evolution), QQ-CATV (CAT + total variation), and the proposed QQ-CCTV (temporal clustering, tissue composition, and total variation) in a simulated stroke data set. The numbers indicate mean absolute error (MAE; black) and mean SD (MSD; white). On average, QQ-CCTV provides the greatest accuracy (smallest MAE 4.3%) and precision (smallest MSD 1.8%). OEF_{avg} and OEF_{std} indicate the average and SD OEF maps among five trials, respectively

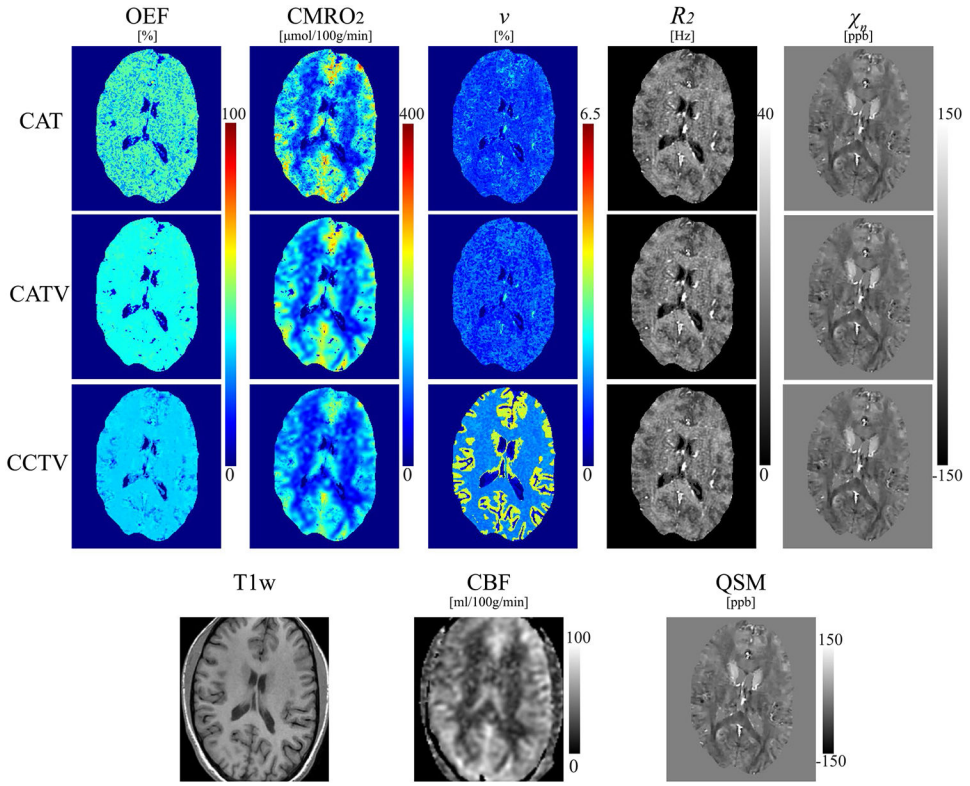

FIGURE 2.

Comparison of OEF, cerebral metabolic rate of oxygen ($CMRO_2$), v, R_2, and χ_n maps among QQ-CAT, QQ-CATV, and QQ-CCTV in a healthy subject. The QQ-CCTV map shows a less noisy OEF and a clearer v contrast between cortical gray matter and white matter. The corresponding anatomy as depicted on a T_1-weighted image, cerebral blood flow (CBF) map, and susceptibility map are shown for reference

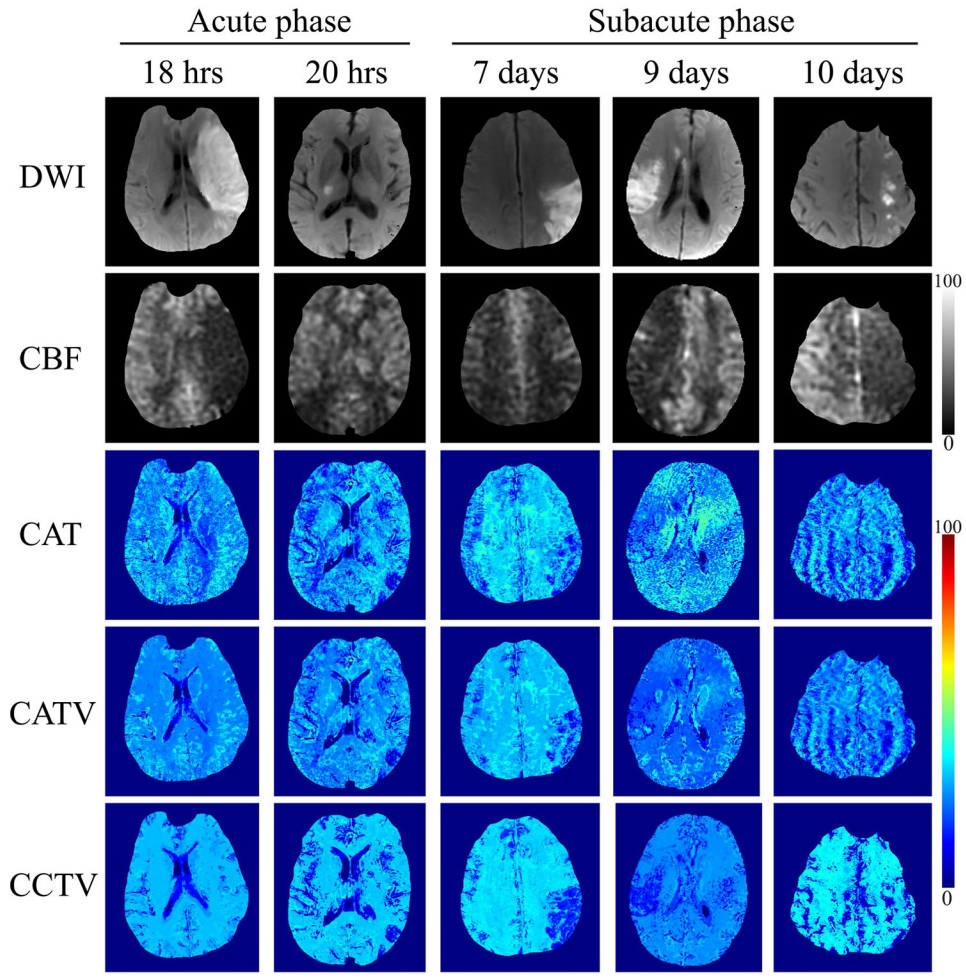

FIGURE 3.

Comparison between the OEF obtained by QQ-CAT, QQ-CATV, and QQ-CCTV in 6 stroke patients imaged between 18 hours and 10 days post stroke onset. The QQ-CCTV shows more uniform OEF maps except for DWI-defined lesions compared with QQ-CAT and QQ-CATV. In the subacute phase patients, low OEF areas in QQ-CCTV agree better with DWI-defined lesions. The CBF maps are shown for reference in units of mL/100 g/min

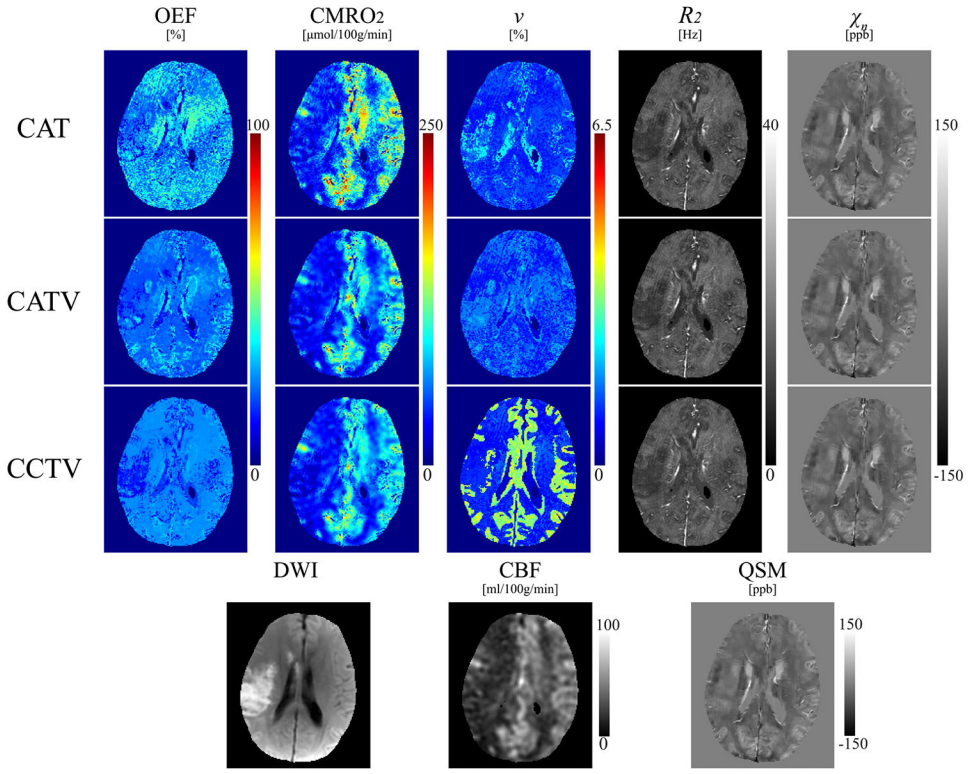

FIGURE 4.

Comparison of OEF, $CMRO_2$, v, R_2, and χ_n maps from QQ-CAT, QQ-CATV, and QQ-CCTV in a stroke subject (9 days following onset). The QQ-CCTV map shows a low OEF area that agrees better with the DWI-defined lesion than QQ-CAT and QQ-CATV

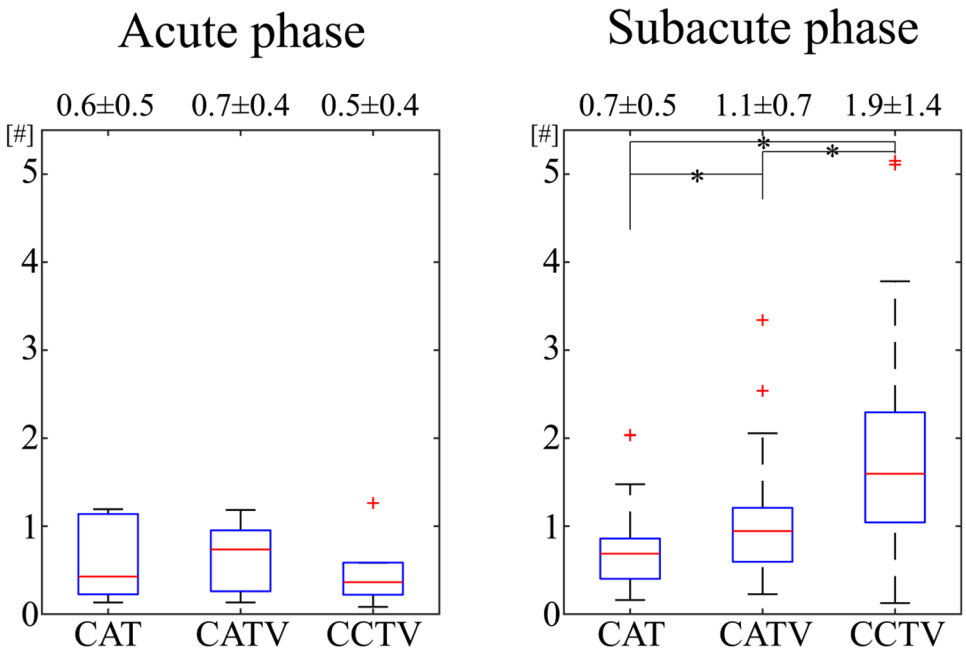

FIGURE 5.

Boxplots of OEF contrast-to-noise ratio (CNR) between the lesion and contralateral side in acute (6-24 hours post onset, $N = 6$) and subacute (1-14 days post onset, $N = 27$) ischemic stroke patients. The number indicates average ± SD. Asterisk (*) indicates a significant difference ($P < .05$). Compared with QQ-CAT and QQ-CATV, QQ-CCTV provided significantly greater CNR in the subacute phase, whereas the CNR was not significantly different in the acute phase